Ultra Low Temperature Scanning Tunneling Microscopy on Turbostratic Graphene

Anmol Arya
Roll No: MS16105

A dissertation submitted for the partial fulfilment
of BS-MS dual degree in Science

Under the guidence of
Dr. Goutam Sheet

April 2021

Indian Institute of Science Education and Research Mohali
Sector - 81, SAS Nagar, Mohali 140306, Punjab, India

Certificate of Examination

This is to certify that the dissertation titled **"Ultra Low Temperature Scanning Tunneling Microscopy on Turbostratic Graphene"** submitted by **Anmol Arya** (Reg. No. MS16105) for the partial fulfillment of BS-MS dual degree programme of the Institute, has been examined by the thesis committee duly appointed by the Institute. The committee finds the work done by the candidate satisfactory and recommends that the report be accepted.

Dr. Yogesh Singh Dr. Sanjeev Kumar Dr. Goutam Sheet
(Supervisor)

Dated: 30.04.2021

Declaration

The work presented in this dissertation has been carried out by me under the guidance of Dr. Goutam Sheet at the Indian Institute of Science Education and Research Mohali.

This work has not been submitted in part or in full for a degree, a diploma, or a fellowship to any other university or institute. Whenever contributions of others are involved, every effort is made to indicate this clearly, with due acknowledgement of collaborative research and discussions. This thesis is a bonafide record of original work done by me and all sources listed within have been detailed in the bibliography.

Anmol Arya
(Candidate)

Dated: April 30, 2021

In my capacity as the supervisor of the candidate's project work, I certify that the above statements by the candidate are true to the best of my knowledge.

Dr. Goutam Sheet
(Supervisor)

Acknowledgement

First and foremost, I would like to thank my thesis supervisor Dr. Goutam Sheet, without whose help and supervision, this thesis would have never been possible. The discussions that I had with him has enhanced my capabilities as a researcher. His enthusiasm for work and his way of explaining Physics has encouraged me a lot to keep my interest alive in this field. His way of teaching has always given me a new insight into the topic and concepts.
I would like to express my sincere gratitude to the members of thesis committee, Dr. Yogesh Singh and Dr. Sanjeev Kumar for their valuable comments and intriguing questions during my thesis evaluation. I am indebted to Dr. G.U. Kulkarni for providing the Turbostratic Graphene and allowing us to study the sample.
I wish to thank all the members of SPIN lab, without them i wouldn't have survived a single day in the Lab. A special thanks to Mr. Soumyadip(*dilution Devta*) for teaching me the basics of cryogenics and STM from scratch along with the art of cracking jokes and Ms. Mona(*dilution Devi*) for being such a nice friend, teacher and moral supporter at times of distress. I would like to thanks Ms. Deepti(*stm Devi*) and Ms. Aastha(*afm Mata*) for bearing me and my silly questions and allowing me to work with them on STM. I would like to thank Mr. Ritesh(*noisy nana*), Mr. Sandeep(*1K chacha*), Mr. Soumya Datta, Ms. Monika(*litho lali*) and Mr. Shelender for their help and for being available at all times when i needed them.
I would like to thank my My friends Jasskaran bhaia for giving me some valuable advices, Saswat for stealing my food and also for useless but entertaining conversations, Tejandra for always being their to save me from trouble, Saurav for being a positive friend, Aman for being a true friend, Prathamesh for being a smart friend, Praveen and Jayant for being entertaining and supportive juniors, Sachu for having a long conversation about anything and everything, Navya for being a sweet friend and Gouri for being my besty. A special thanks to Ms.Vamika for making my last year of college a memorable one.

I would like thank my papa, Mummy and my didi for being my backbone all the time and for always encouraging me to take the right decision. Thank you for being a lifeline at the time of distress. I would like to thank all of my family members for their constant support and for believing in me.

I wish to thank all my well wishers.

Anmol Arya

MS16105

IISER Mohali.

List of Figures

List of abbreviations

STM:Scanning Tunneling Microscopy

MFM:Magnetic Force Microscopy

PCARS:Point contact Andreev Reflection Spectroscopy

T-SGL:Turbostratically Single layer Graphene

DOS:Density of States

LLC:Load Lock Chamber

EC:Exchange Chamber

PC:Preparation Chamber

FFT: Fast Fourier Transform

LPF: Low pass filter

PMF: Pseudo Magnetic field

PLL: Pseudo Landau Levels

VD: Voltage divider

Contents

Abstract

Graphene has always been a fascinating material because of its extraordinary properties. These properties can be seen vividly when graphene is suspended. A new multilayer graphene system has been reported as turbostratic graphene, where every layer is decoupled from the other layer. Raman spectra of this system show similar spectra as that of suspended graphene. Graphene produces a pseudo magnetic field in the presence of strain, which reconstructs the band structure into pseudo-Landau levels. However, It is challenging to construct a particular strain texture that can produce a pseudo magnetic field over a wide area in an experimental setting. This sample provides a possible pathway to study strain-induced pseudo magnetic fields in suspended graphene in a much more flexible way. In this thesis, I have attempted to investigate properties of turbostratic graphene using Scanning Tunneling Microscopy as well as spectroscopy. A direct measure of the angle between the layers is done using Moire patterns formed as a result of multiple overlaying graphene sheets from scanning tunneling microscopy and a python simulation. We measure the strain-induced pseudo magnetic via the pseudo-Landau levels spectra found by scanning tunneling spectroscopy. We also try to explore the delocalization of the pseudo magnetic field in the areas near the wrinkle. We have attempted to present turbostratic graphene as a new pathway to strain-induced engineering through this study.

Chapter 1

Introduction

The extraordinary optical, mechanical and electronic properties of graphene has always drawn the interest of condensed matter community. These properties of a graphene system, on the other hand, can be easily tuned and observed when the graphene is suspended or free of any substrate effect[MDP$^+$15]. The existence of a non-uniform strain in graphene impacts the two sub-lattices of bipartite graphene differently and moves the Dirac cones in opposite directions, resulting in pseudo magnetic fields (PMF $_s$).The reconstruction of band structure into Pseudo Landau levels is possible thanks to these PMFs findings. Creating certain stresses on graphene structures, on the other hand, has always been difficult. Creating a strain texture that can produce PMFs over a wide region is extremely difficult at the experimental level.[JMD$^+$17]

Recently, a new type of multilayer graphene has been reported as turbostratically single layer graphene prepared by Professor G.U.Kulkarni's group[MDP$^+$15]. In this system every layer of graphene is turbostratically decoupled from the other layer solving the problem of substrate influence free graphene. Along with suspended graphene layer, the system also have mechanical strains making it a perfect candidate to study delocalized strain induced PMF$_S$.(More detail about the sample is given in Chapter3). In this thesis, I have used Scanning Tunnneling Microscope(STM) to investigate the the generation of Pseudo Landau levels at regions of wrinkle on the sample along with the topographical analysis of the sample. I utilized topographical data to extract information about Moire pattern as well as wrinkles and found that the surface topography is a contribution of three consecutive layers. I also utilized Moire pattern to figure out the approximate angle between the graphene layers.The spectroscopic analysis resulted in Landau level peaks in density of states(DOS)

vs. V which is very similar to other experimental results presented in literature and these peaks correspond to a PMF_s of 3 Tesla.

1.1 Scanning Tunneling Microscopy

The first scanning tunneling microscope was invented by Binning and Rohrer in the year 1982. Scanning tunneling microscopy is a technique that uses vacuum quantum tunneling to facilitate surface studies at a nanometer level. It contains an atomically sharp conducting tip for scanning and a flat conducting sample. A voltage V is applied between the tip and the sample. As a result, electrons "tunnel" or jump from the tip to the flat surface(vice-versa, depending on the bias given to the sample). This tunneling gives rise to a current (also known as tunneling current) that can be measured as a function of position(X,Y) and applied bias.[Hof03] A schematic of the STM tip and sample is shown in figure1.1.

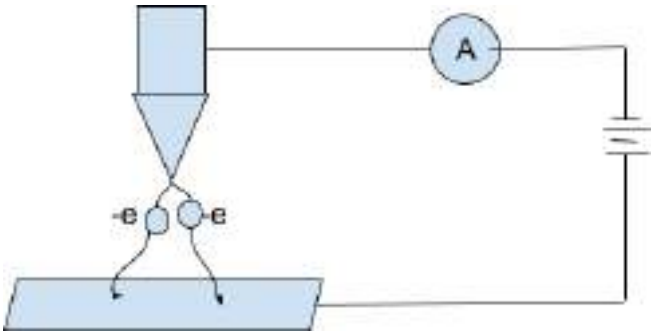

Figure 1.1: schematic of tip and sample with a bias V applied between them.

1.1.1 Tunneling current

The tunneling current can be estimated by using time-dependent perturbation theory. If the sample is given negative bias then the Fermi level of the electrons in the sample will shift up with respect to the tip electrons. This is illustrated in figure1.2.

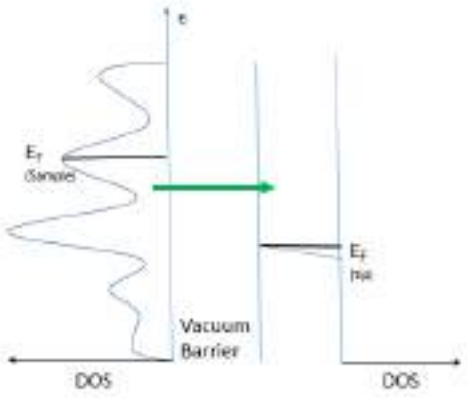

Figure 1.2: Green arrow depicts the tunneling of electrons as a result of negative bias given to the sample. The density of states is along X-axis, and energy is along Y-axis. All the states below the Fermi level(sample and tip) are filled.

As a result of this shift in the Fermi surface, the electrons from the sample will tunnel towards the tip. The current generated from the tunneling of electrons for the state having energy ϵ is:

$$I_S \rightarrow_T = -2e\frac{2\pi}{\hbar}|\alpha|^2(\rho_S(\epsilon)\cdot f(\epsilon))\cdot(\rho_T(\epsilon+eV)[1-f(\epsilon+eV)]) \tag{1.1}$$

Where $|\alpha|^2$ is the tunneling matrix element, $(\rho_S(\epsilon)\cdot f(\epsilon))$ are filled sample states for tunneling from sample to tip, $(\rho_T(\epsilon+eV)[1-f(\epsilon+eV)])$ are empty tip states for tunneling to tip, $\frac{2\pi}{\hbar}$ is given by time dependent perturbation theory, -e is the electronic charge, 2 factor is a result of spin consideration, $\rho_{T(S)}$ corresponding to the density of states of the tip(sample) and (ϵ) is the Fermi distribution.[Hof03] Although the majority of tunneling current will be from sample to tip(considering negative bias), there will be a contribution from tip to sample tunneling current.

$$I_S \rightarrow_T = -2e\frac{2\pi}{\hbar}|\alpha|^2(\rho_T(\epsilon+eV)\cdot f(\epsilon+eV))\cdot(\rho_S(\epsilon)[1-f(\epsilon)]) \tag{1.2}$$

Summing both equations 1.1 and 1.2 and integrating overall energies(ϵ), we get the total tunneling current from sample to tip:

$$I_S \rightarrow_T = \frac{4\pi e}{\hbar}\int_{-\epsilon_{F(Tip)}}^{\infty} d\epsilon|\alpha|^2\rho_S(\epsilon)\cdot\rho_T(\epsilon+eV)\Big[f(\epsilon)[1-f(\epsilon+eV)]-f(\epsilon)+eV)\cdot[1-f(\epsilon)]\Big] \tag{1.3}$$

After simplifying the expression, the range under which tunneling current is integrated is from $-eV < \epsilon < 0$(for negative bias). Therefore the total tunneling current in the range $eV < \epsilon < 0$ is given by:

$$I_S \rightarrow_T = \frac{4\pi e}{\hbar} \int_{-eV}^{0} d\epsilon |\alpha|^2 \rho_S(\epsilon) \cdot \rho_T(\epsilon + eV) \tag{1.4}$$

The material of a tunneling tip is preferred in such a way that it has a flat density of states under the range of Fermi surface of the sample under study. In this thesis, all the measurements were taken with a tungsten tip, prepared by electrochemical etching(discussed in chapter 2). The tunneling current expression gets even more simplified by choosing such kind of tip.

$$I = \frac{4\pi e}{\hbar} \rho_T(0) \int_{-eV)}^{0} d\epsilon |\alpha|^2 \rho_S(\epsilon) \tag{1.5}$$

The above expression can be further simplified by involving Bardeen's assumptions. Bardeen proved that 1)the density of states of both sample and tip are independent, 2) the eigenfunctions of both sample and tip falls off exponentially in the vacuum, 3) the overlap between the wavefunction of tip and sample is insignificant, as a result, the matrix element does not change. So, $|\alpha|$ can be taken out of the integral.

$$I = \frac{4\pi e}{\hbar} \rho_T(0) |\alpha|^2 \int_{-eV)}^{0} d\epsilon \rho_S(\epsilon) \tag{1.6}$$

To get the tunneling probability which is nothing but $|\alpha|$, we use WKB approximation by assuming vacuum gap as a square well with a tilt of the order of few hundred millivolts. The tilt is the result of applied bias, while the remaining height of the barrier corresponds to the sample's work function. This is shown in the figure1.3 below.

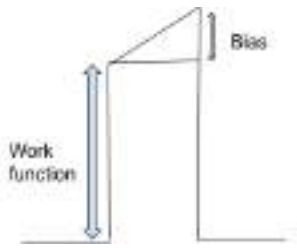

Figure 1.3: Schematic of potential profile showing work function(ϕ) and applied bias(V)

As a result of WKB approximation and assumption that $\phi >> eV$ we get,

$$|\alpha|^2 = e^{-2\gamma} \tag{1.7}$$

where

$\gamma = \int_0 h\sqrt{\frac{2m\phi}{\hbar^2}}dx$

m = mass of electron

h = tip-sample separation

ϕ = height of the barrier

This implies that

$$I \propto e^{-2h\frac{\sqrt{2m\phi}}{\hbar}} \tag{1.8}$$

Furthermore, the above expression can be deduced that with the change in the tip-sample separation(h) there will be a change in the tunneling current and higher work function ϕ results higher resolution.

At last, the tunneling current in its most simplified form can be written as:

$$I \approx \frac{4\pi e}{\hbar}\rho_T(0)e^{-2h\frac{\sqrt{2m\phi}}{\hbar}}\int_{-eV}^{0}\rho_S(\epsilon)d\epsilon \tag{1.9}$$

1.1.2 Topography through STM

One of the most common yet powerful measurements performed worldwide by using STM is the surface topography. The tip is moved in the raster format over the sample surface at a fixed bias voltage $-V_{set}$. 1) A feedback loop is turned on that controls the Z-piezo(more detail is given in chapter 2) movement or voltage to the z-piezo to keep the set current I_S constant. This voltage change in the Z-piezo supply helps effectively map the height of the sample(topography). 2) The other way to map the sample surface is by constant height mode. In this mode, the tip's height is kept constant, and the change in the tunneling current is measured as the tip moves in the raster format. Then this change in current is mapped to get the topography. Note that the tunneling current that we receive while performing topography measurements is from the electrons below Fermi level energy and above the -eV energy. And we cannot increase the bias voltage to a substantial value to get a better image because then our tunneling approximation will break down.

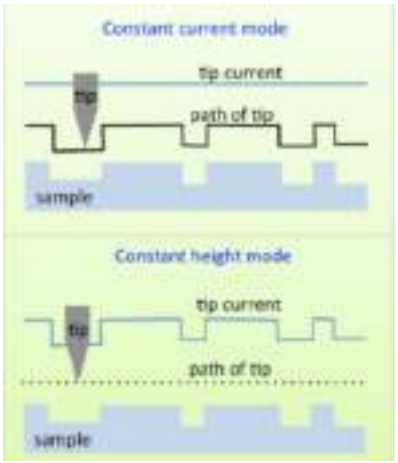

Figure 1.4: Constant current mode and constant height mode in STM.

1.1.3 Spectroscopy through STM

To understand the concept of spectroscopy, one has to first understand density of states. From equation 1.9 it is clear that the current that is measured is proportional to the integral of density of states over the range $-eV < \epsilon < 0$. In other words, as we measure the tunneling current, we also measure the integrated density of full states below the Fermi level(for negative bias). But we are interested in knowing only the density of states to map out the whole density of states curve. One way to do it is by simply taking the numerical derivative of integrated density of states vs V curve. But this method is not efficient as it generates a lot of noise in the data. This is shown in figure1.5.

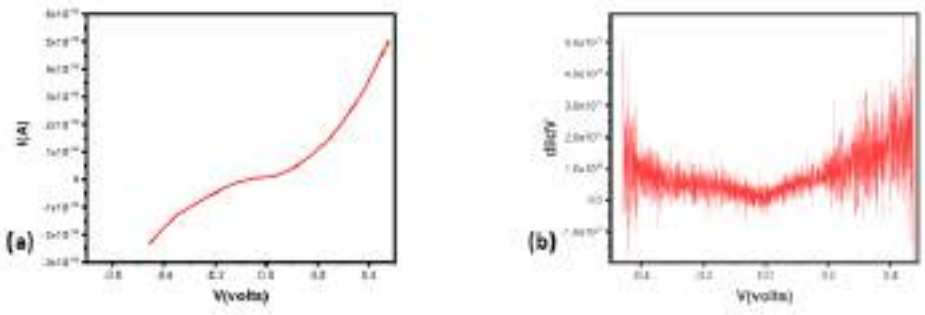

Figure 1.5: (a) Graph between tunneling current and applied bias. (b) Numerical derivative of graph (a) with a lot of noise.

To overcome from this problem, the bias voltage is modulated by a small AC voltage

dV(few millivolts) with the help of a lock-in amplifier. A small change dV generates a small change dI at the same frequency. This ratio $\frac{dI}{dV}$ is known as conductance $\sigma(V)$.

$$\sigma(V) = \frac{dI}{dV} \propto DOS(eV) \tag{1.10}$$

So, with the help of a lock-in amplifier and varying bias voltage, we can span the whole density of states curve.

Now, to generate the DOS vs. energy curve(spectroscopy) at a point, the tip is set at a fixed height(mostly lower than the height when doing topographic analysis). The bias is swiped over a set range along with the modulated signal dV to generate a plot of DOS vs. energy. This is shown below in figure1.6.

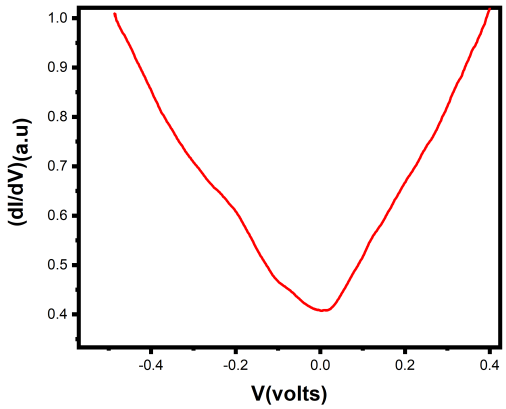

Figure 1.6: Plot between density of states($\frac{dI}{dV}$) vs energy(V) from STM.

One can also generate a conductance map by moving the tip at the same bias with some modulation over the whole space. In any of the DOS measurements, the feedback loop is turned off(except when doing spectroscopy along a line).

Chapter 2

Instruments and technical details

2.1 Vacuum and cryogenics

To probe subatomic features and for clean topography through STM, one must take the system to ultrahigh vacuum and ultra-low temperature. At 10^{-6} torr, which is eight orders of magnitude lower than the atmospheric pressure, we see about one monolayer of dust(unwanted molecules/ atoms) getting deposited per second. And this rate decreases as we go down to lower pressures. It is necessary to take the systems to an ultra-high vacuum state to get a clean topography. Similarly, to probe features like superconducting gap and landau levels, one must take care of thermal noise or Johnson noise. Johnson noise decreases by a factor of $\sqrt{\frac{300}{300\times10^{-3}}} = 10\sqrt{10}$ when the system reaches a 300 milliKelvin temperature.

In this thesis all the measurements were taken utilizing a UHV(ultra high vacuum) Helium3 based cryogenic system(down to 300 milliKelvins) integrated with 11 Tesla superconducting magnet built by UNISUKO(model 1300) equipped with JANIS- He3 cryostat.

a) Vacuum system and sample transfer procedure: The whole system consists of three main chambers along with the STM chamber. All these chambers are illustrated in the figure2.1 given below.

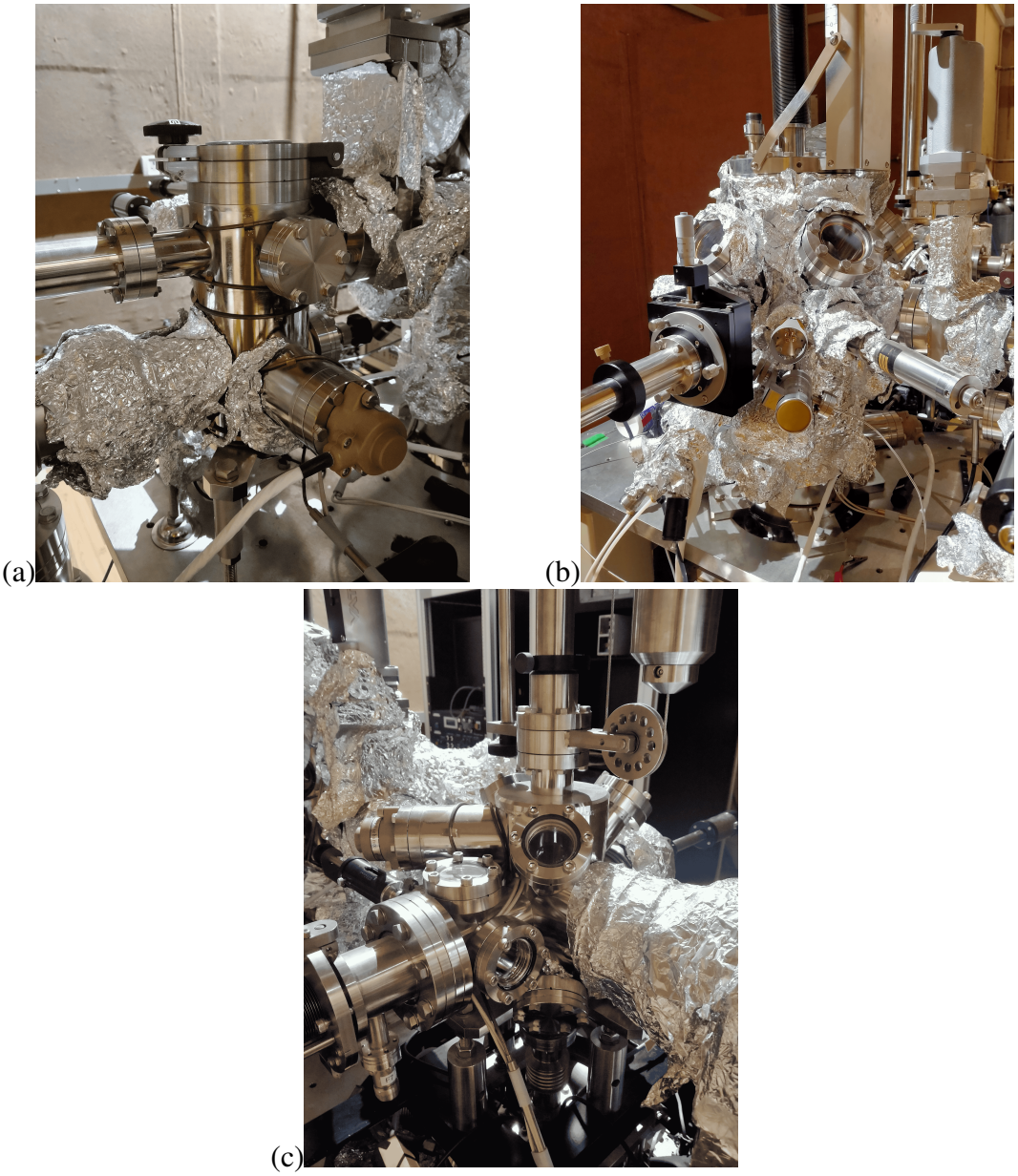

Figure 2.1: (a) Load lock chamber, (b) Preparation Chamber, (c) Exchange Chamber

All the chambers are seperated by a VAT valve and are maintained at UHV($10^{-9}-10^{-10}$mbars) with the help of an ion pump, except the load lock chamber.

The load lock chamber(LLC) is the first stage to transfer a new sample and tip. LLC is small in size, and it is connected by an Edward nEXT-300 Turbomolecular pump(TMP) separated by a pneumatic valve. After transferring the sample or tip inside the LLC it is pumped down to $10^{-8} - 10^{-9}$mbar, and then the VAT valve between the LLC and preparation chamber(PC) is opened to transfer the sample and/or tip to PC. After transferring the sample, the VAT valve is closed. In PC, one can clean the sample by different methods like Argon bombarding and by heating the silicon chip over which the sample is placed. The tip

is cleaned by bombarding an electron beam over it.

Figure 2.2: Tip cleaning system inside PC

After preparing the tip/sample it is transferred to the exchange chamber(EC) maintained at $10^{-9} - 10^{-8}$ using a magnetic manipulator. In EC, it is possible to cleave the sample at low temperature(77 kelvin), which is another way of cleaning the sample.
At last, the sample and/or tip is transferred in the STM chamber(10^{-1}0mbar) using a long magnetic manipulator.

b) STM at 300mK

A brief description of the components of crystat and their working to take the system to 300 milliKelvin is given below:

- Vacuum jacket: It is a vacuum space(holding pressure 10^{-1}mbar) that separates the cryostat's outer region from the inner region. It simply isolates the inner cryostat from outer surroundings, thus minimizing the boil-off of liquid helium4.

- Inner vacuum chamber(IVC): It is a chamber that holds the Inset. An Inset consists of a charcoal pump, 1K pot, helium3 pot, and the STM sample stage. An ion pump continuously pumps IVC to maintain a pressure of $10^{-9} - 10^{-10}$ mbars.

- Helium chamber: It is a chamber where liquid helium4 gets filled. A long narrow capillary passes through this chamber and enters into the 1K pot. A needle valve controls the flow of the capillary.

- 1K pot: It is a small chamber inside an IVC. This small chamber is continuously pumped to create a pressure difference. This pressure difference forces helium4 to

raise through the capillary. By the process of evaporative cooling, 1K pot reaches from 4kelvin to 1kelvin.

- Charcoal pump: It is a pump that helps in condensing helium3 in Helium3 pot. As the system is cooled to 1Kelvin, the charcoal pump also becomes cold. Cold charcoal pump absorbs the gaseous helium3 from the helium3 cylinder attached outside the cryostat. To condense helium3 into the helium pot charcoal pump is heated. Consequently, the charcoal pump releases helium3, and this helium3 passes through a capillary and enters the helium pot. After condensation of helium3, the charcoal pump is again allowed to cool, and as a result, it starts absorbing helium3 from the helium3 pot. Thus, by the process of evaporative cooling helium3 pot reaches a temperature of 300mK.

- STM sample stage: It is the region where the sample is placed. The sample stage is in thermal contact with the helium3 pot as well as with 1K pot. This contact is manually controlled with the help of a heat switch when helium3 reaches 300 mK, the sample stage also reaches 300mK.

2.2 Data acquisition for topography and spectroscopy

It is essential to take care of different noises from your data to get clean and noise-free measurements. In this thesis, all the measurements were taken using the R9 controller from RHK technology interfaced with STM. R9 suppresses the electrical noise to a reasonable extent. R9 consists of four lock-in amplifiers (0-100kHz), several voltage sources(-10V to 10V), high/low pass filter, two PLLs, twenty DACs, four digital oscillators, and spectrum analyzers[DAS19]. R9 is controlled by the Icon-based program language(IHDL). In this section, I have tried to explain the basic electronics and working of different instruments to acquire topographic and spectroscopic data from STM without going into the in-depth details.

a) Piezo scanner: Piezoelectrics are materials that respond to electrical signals by converting electrical energy to mechanical energy. They expand/contract accordingly to the applied bias. The piezo scanner in STM consists of two parts. (i) Scanner for fine movement in X and Y direction and (ii) walker for course movement in the Z direction. The initial distance between the sample and tip is approximately 1mm. It is a considerable distance for a

scanner piezo to cover. It will take at least 24 hours for a scanner to reach up to a distance of a few Angstrom(the scanning regime). To get away with that problem, a Z-piezo walker is attached to the tip system. This Z-piezo allows the tip to move towards the sample in lesser time(4-5 hours). It is kept in mind that the set current value is not too high when the tip is under course approach mode. Otherwise, there are chances of tip to crash. The tip is generally approached with the help of a course approach mode up to a limit of tunneling current≈1.9nA. To move the tip further, the scanner is used. It works under the name of the USM approach in R9 software. The whole mechanics for piezo is controlled by PMC-100 controller interfaced with R9 controller[DAS19].

b) Topography: R9 gives a certain bias to the sample. This bias is preamplified using a preamplifier(R9 IVP preamp) and filtered by a high voltage filter(530kHz) to remove high-frequency noise from the input signal. An output tunneling current is measured using a Femto DLPCA-200 current amplifier(gain from $10^3 to 10^{11}$ V/A) which converts the output current to voltage and amplifies it. Given below is the schematic(figure) of the basic circuit of STM for topography and spectroscopy.

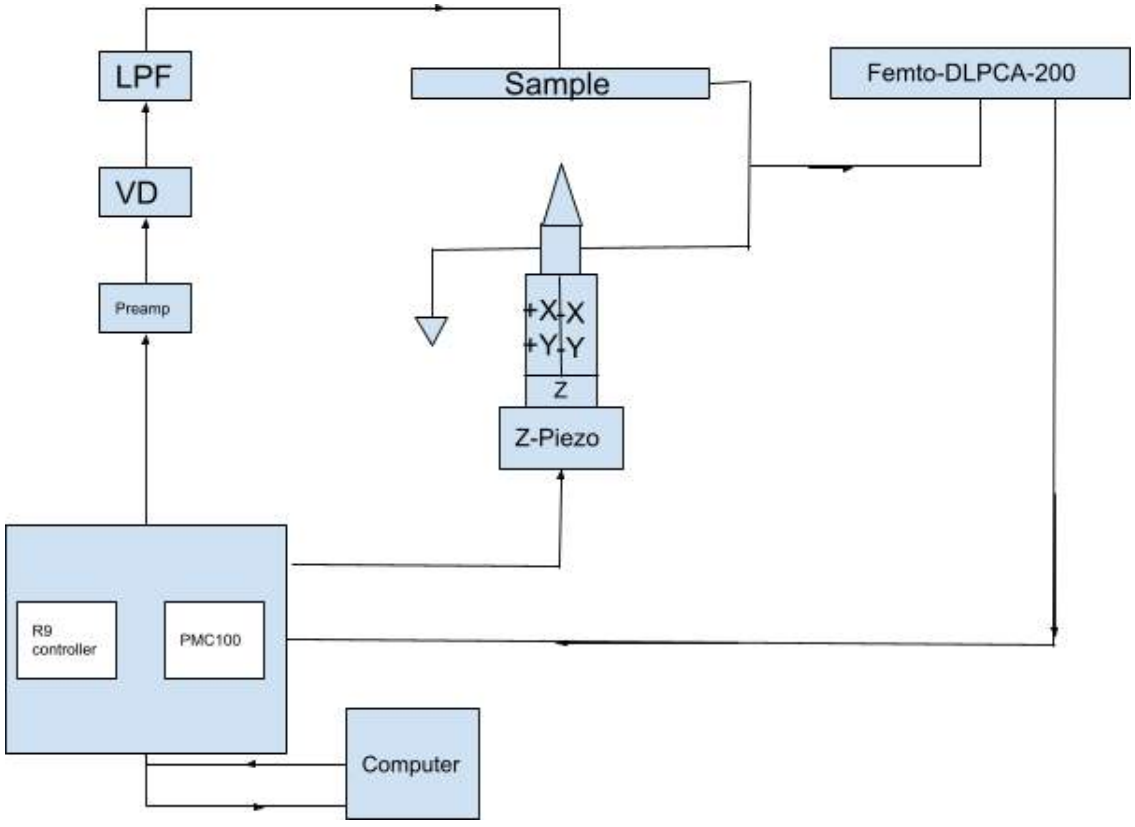

Figure 2.3: Schematic of STM with basic electronic components

c)Spectroscopy: As mentioned earlier in chapter 1 that a small change dV generates a small change dI, and density of states($\frac{dI}{dV}$) vs. V(energy) can be plotted. But it is not as simple as it looks. During the topographic measurement, the sample and the tip are biased by specific voltage. There is no capacitive current involvement as the bias that we are giving is a DC bias, and the current that is measured is purely tunneling current. On the other hand, In the case of $\frac{dI}{dV}$ measurement, the sample is biased with a DC voltage modulated with an AC voltage given by a lock-in amplifier.

$$I(V = V_{DC} + V_{AC}cos(\omega t)) = I(V_{DC}) + \frac{dI}{dV}V_{AC}cos(\omega t) \quad [byTaylorexpansion] \quad (2.1)$$

Now, the critical point to note is that while performing the $\frac{dI}{dV}$ measurements, the capacitive current comes into the picture(since the bias is modulated). But we want to remove this capacitive current and get a pure tunneling current. To solve this problem, the phase rotation of the modulating signal is performed. With the help of the phase offset function in R9 software, the lock-in amplifier is allowed to automatically remove the artifacts in the tunneling current caused due to the capacitive coupling of the tip and sample.The bias voltage modulation is turned on, and the phase offset of the lock-in is rotated from 0^o to 360^o. This data is plotted in real-time. Selecting the peak value from the above graph and selecting the offset button to set it to -90^o will ultimately remove the capacitive contribution in the current.

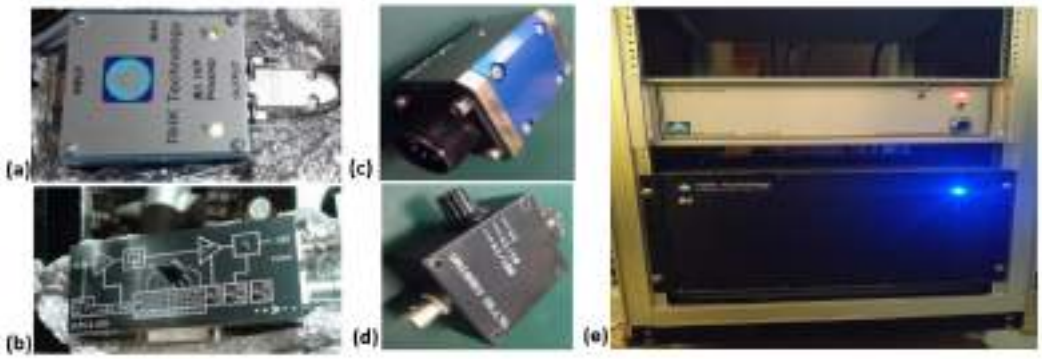

Figure 2.4: (a) Pre amplifier, (b) DLPCA-200, (c) Low pass filter, (d) voltage divider, (e) R9 controller and PMC100,

2.3 STM Tip

STM tip plays a crucial role in getting an atomic resolution image. It is necessary to have an atomically sharp tip. In this thesis, all the measurements were taken by a tungsten tip prepared by electrochemical etching. Tungsten(W) has a flat density of states near the Fermi- level, and that makes it a suitable material for STM tip.

To prepare a tip by electrochemical etching first, a wire of diameter 0.5mm and length 0.8-1.2cm is cut, then this wire is scratched with P8000 grade sandpaper to remove the oxide layers roughly. This scratched tip is cleaned with ethanol, and then it is fixed at the tip holder(one of the electrodes). A 1.2N KOH solution is prepared. For the other electrode, a ring-shaped platinum wire is used. Both the electrodes are dipped in the KOH solution, and a bias of about 10V is supplied. To control the etching automatically, a current feedback loop with a circuit breaker is utilized. Once the current reaches a set value, the etching stops. As soon as the etching stops, a buzzer starts beeping. The tip is immediately taken out of the tip holder and dipped first into distilled water for thirty seconds, then into ethanol for another thirty seconds. This process is done to prevent any oxidation on the newly formed tip. Finally, the apex of the tip is examined under an optical microscope. It is then transferred to the PC chamber via LLC where it is treated by an electron beam to remove any oxide layer and modify the tip apex.

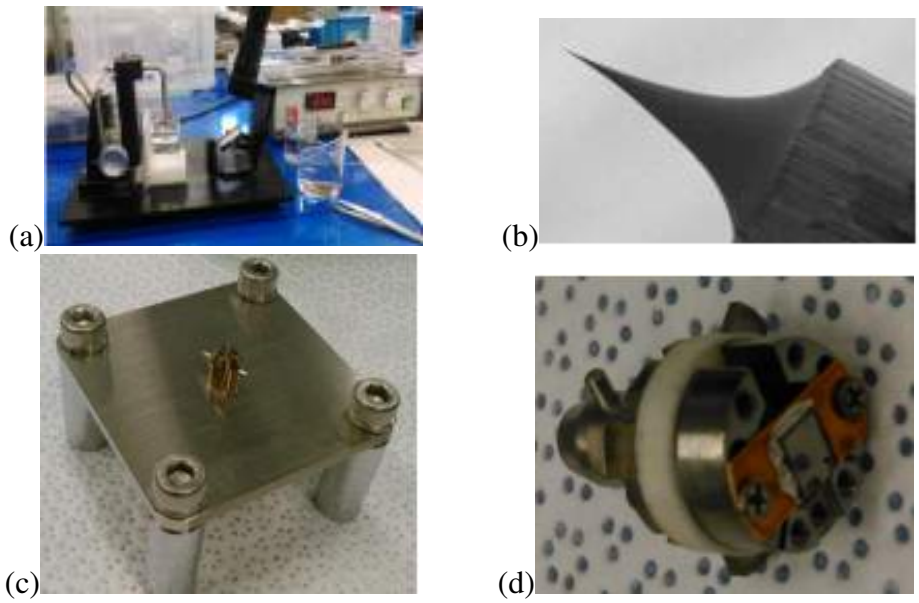

Figure 2.5: (a) Setup for electrochemical etching, (b) Image of prepared tip in optical microscope, (c) Tip holder, (d) Sample holder

Chapter 3

STM studies on Turbostratically single layer graphene

3.1 Graphene

Monolayer

Graphene is 2D material composed of sp^2 hybridized carbon atoms arranged in a honeycomb lattice possessing some extraordinary physical, optical and electronic properties.[CNGP+09, Gei07] The electronic configuration of carbon atom is $1s^2 2s^1 2p_x^1 2p_y^1 2P_z^1$ with four unpaired electrons in separate orbitals resembling the tetravalent carbon atoms. It is the mixing of 2s and 2p atomic orbitals that results in three inplane hybridized orbitals as shown in figure(1.7).

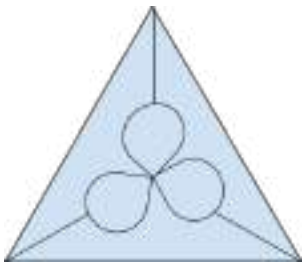

Figure 3.1: Three in-plane hybridized orbitals

These orbitals are at 120^o with each other and are the reason for hexagonal(honeycomb) lattice structure.[Dat20] The unit cell of graphene consists of two lattice sites, also known as a bipartite lattice, of two triangular sub-lattices.

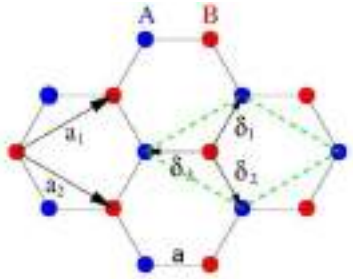

Figure 3.2: Honeycomb lattice of graphene with two lattice sites A and B[CNGP$^+$09]

Many of the interesting properties of graphene can be understood with the help of energy dispersion relation. Considering the tight binding hamiltonian,

$$\hat{H} = -\alpha \sum_{<l,m>} (p_l^* q_m + q_m^* p_l) \tag{3.1}$$

Where l, m represents the sites in sublattices A and B respectively, the $p_l^*(p_l)$ represents the fermionic creation(annihilation) operators that creates(annihilates) the electron at position r_l(site A), and similarly q_m and q_m^* at site B. The above hamiltonian can be rewritten by utilizing our nearest neighbour assumption as,

$$\hat{H} = \sum_{i\epsilon A} \sum_{\delta} (p_l^* q_{l+\delta} + q_{l^*+\delta}^* p_l) \tag{3.2}$$

where δ can take values

δ_1= $\frac{a}{2}$(1,$\sqrt{3}$)

δ_2= $\frac{a}{2}$(1,-$\sqrt{3}$)

δ_3= -$\frac{a}{1}$(1,0)

with 'a' being the lattice constant. Here $q_{l^*+\delta}^*$ will create an electron at position r_l+_δ on site B. Now using

$$p_l^* = \frac{1}{\sqrt{\frac{N}{2}}} \sum_k exp(i\vec{k} \cdot \vec{r}) p_k^* \tag{3.3}$$

and writing in the similar fashion for all other fermionic operator in the hamiltonian we get,

$$\hat{H} = -\alpha \sum_{\delta,k} (exp(-i\vec{k} \cdot \vec{\delta}) p_k^* q_k + exp(i\vec{k} \cdot \vec{\delta}) p_k q_k^*) \tag{3.4}$$

As we can see the above hamiltonian can be written in matrix form as,

$$\begin{pmatrix} p_k^* & q_k^* \end{pmatrix} \begin{pmatrix} 0 & -\alpha f(k) \\ -\alpha f^*(k) & 0 \end{pmatrix} \begin{pmatrix} p_k \\ q_k \end{pmatrix} \tag{3.5}$$

Let us define a matrix S(k) and Φ as

$$S(k) = \begin{pmatrix} 0 & -\alpha f(k) \\ -\alpha f^*(k) & 0 \end{pmatrix} and \quad \Phi = \begin{pmatrix} p_k \\ q_k \end{pmatrix} \tag{3.6}$$

Therefore,the Hamiltonian can be written as

$$\hat{H} = \sum_k \Phi^* S(k) \Phi \tag{3.7}$$

But we are in interested in knowing the eigen values of the matrix S(K) which will give us the dispersion relation and information about bands. The eigenvalues of S(k) matrix are,

$$\epsilon_\pm = \pm\sqrt{f^*(k)f(k)} \tag{3.8}$$

This expression can be further simplified by puttingδ_1, δ_2 and δ_3 in f(k)as,

$$f(k) = exp(i\vec{k} \cdot \vec{\delta_1}) + exp(i\vec{k} \cdot \vec{\delta_2}) + exp(i\vec{k} \cdot \vec{\delta_3}) \tag{3.9}$$

$$f(k) = exp(-k_x a)[1 + 2cos(\frac{\sqrt{3}}{2}k_y a)exp(3ik_x\frac{a}{2})] \tag{3.10}$$

At last we get the dispersion relation as shown in equation 3.11.

$$\epsilon_\pm = \pm\alpha\sqrt{1 + 4cos^2(\frac{\sqrt{3}}{2}k_y a) + 4cos(\frac{3}{2}k_x a)cos(\frac{\sqrt{3}}{2}k_y a)} \tag{3.11}$$

Figure 3.3 shows the 3D plot of the dispersion relation shown in equation(3.11).

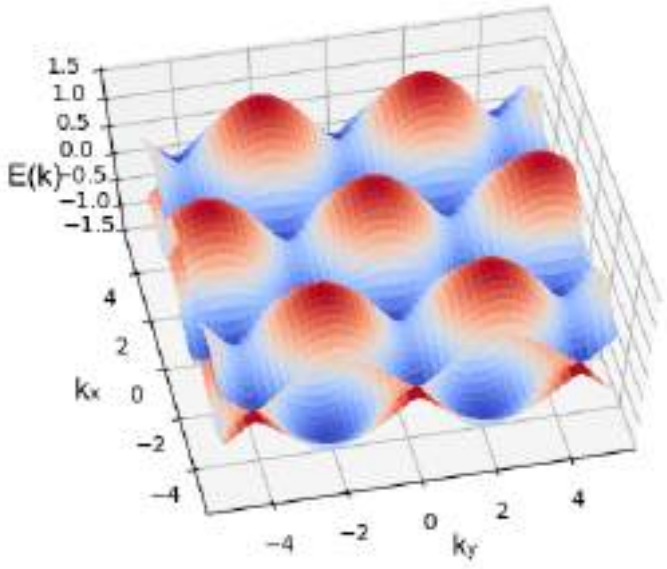

Figure 3.3: Dispersion relation of graphene

It is visible in the plot that there are two bands and degenerate at some points. These are K and K' points. Around these points, the energy dispersion is characterized by two cones(Dirac cones), and the relationship becomes linear.

$$\epsilon_{\pm}(j) = v_F|j| \tag{3.12}$$

with low energy effective Dirac Hamiltonian as

$$\hat{H}(p) = V_F \sigma \cdot p \tag{3.13}$$

where $V_F = \frac{3a\alpha}{2}$, σ is the Pauli matrices and p is the momentum. One can easily prove the linear dispersion by perturbing the dispersion relation given in equation(3.11) around the K=k-j point. It is because of this linear dispersion that graphene became an interesting material to study. In the vicinity of these K and K' valleys, the electrons act as massless fermions moving with Fermi velocity.

Bilayer

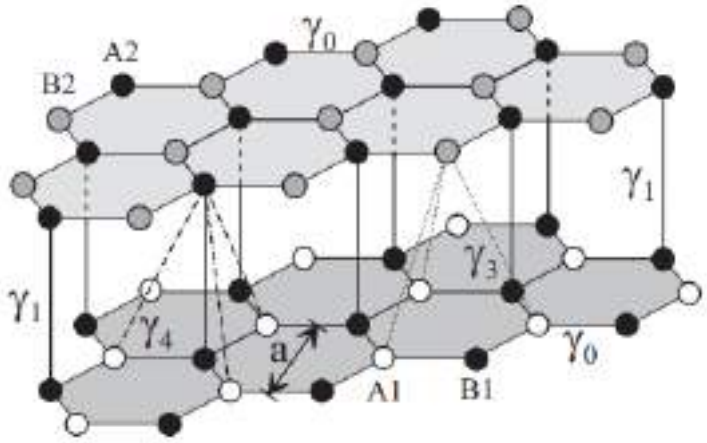

Figure 3.4: Schematic of bilayer graphene[MK13]

The unit cell of bilayer graphene has four atomic sites labelled j= A1, B1, A2, B2. The slanezewski Weiss-Mclure(SWM) model is used to modify the above matrix S(k):

$$H_b = \begin{pmatrix} \epsilon_{A1} & -\gamma_o f(k) & \gamma_4 f(k) & \gamma_3 f^*(k) \\ -\gamma_o f^*(k) & \epsilon_{B1} & \gamma_1 & \gamma_4 f(k) \\ \gamma_4 f^*(k) & \gamma_1 & \epsilon_{A2} & -\gamma_o f(k) \\ -\gamma_3 f(k) & \gamma_4 f^*(k) & -\gamma_4 f^*(k) & \epsilon_{B2} \end{pmatrix} \tag{3.14}$$

where, $\gamma_o = \langle \phi_{A1} | \, H \, | B_1 \rangle$ = - $\langle \phi_{A2} | \, H \, | B_2 \rangle$

$\gamma_1 = \langle \phi_{A2} | \, H \, | \phi_{B1} \rangle$

$\gamma_3 = - \langle \phi_{A1} | \, H \, | \phi_{B2} \rangle$

$\gamma_3 = - \langle \phi_{A1} | \, H \, | \phi_{A2} \rangle$

$\epsilon_i = - \langle \phi_i | \, H \, | \phi_i \rangle$; i=A1, A2, B1, B2

The upper left and lower right square 2×2 blocks of H_b are simple monolayer generation terms[MK13]. Sites B1 and A2 are classified as vertical coupling dimer sites (straight coupling). The $gamma_1$ parameter represents the pairing between pairs of orbitals on dimer sites. In-plane hopping is defined by terms that do not include f(k). Interlayer coupling between non-dimer orbitals A1 and B2 is defined by γ_3, while interlayer coupling between dimer and non-dimer orbitals A1 and A2 or B1 and B2 is described by γ_4. Since the model accounts for one $2p_z$ orbital on each of the four atomic sites in the unit cell, there are four bands: two conduction bands and two valence bands. Each pair is separated by an energy of the order of the interlayer spacing γ_1 ≈0.4 eV over the majority of the Brillouin region. Near the K lines, an energy of the order of the interlayer coupling γ_1 splits one conduction band and one valence band apart from zero energy, while two bands meet at zero energy. The 'split' bands result from heavy coupling (via interlayer coupling γ_1) of the orbitals on the dimer B1 and A2 sites, while the 'low-energy' bands result from hopping between the non-dimer A1 and B2 sites. The Fermi level in pristine bilayer graphene is located where the two low-energy bands meet, making this area important for studying electronic properties. Only in the vicinity of the Brillouin zone corners K_+ and K_- is the tight binding hamiltonian H_b correct. Eliminating the components in the Hamiltonian related to the orbitals on dimer sites B1, A2 results in an efficient two-component Hamiltonian representing the orbitals on non-dimer sites A1, B2, and hence the two bands that approach each other at zero energy. At last the effective two band hamiltonian is given by :

$$H_b = h_0 + h_w + h_4 + h_\delta + h_U + h_{AB} \tag{3.15}$$

Massless chiral electrons are defined by the first term, h_0. At low energies, it usually governs, and the other terms in H_b can be thought of as perturbations of it. The second term h_w E incorporates 'trigonal warping,' a triangular distortion of the Fermi circle around each K point. Terms h_U and h_{AB} create a band disparity between the conduction and valence bands, with ± 1 on the diagonal, while h_4 and h_δ introduce electron-hole asymmetry into the band configuration.[Theoritical details about bilayer graphene can be found in [MK13]

]

3.2 Landau levels and pseudo magnetic fields in graphene systems

When a free electron is placed in a magnetic field perpendicular(Z direction) to the motion it follows a cyclotron orbit. The corresponding hamiltonian is given by:

$$H = \frac{1}{2m}(p_{ox}^2 + p_{oy}^2 + p_z^2) \quad ; p_{oi} = p_i - eA_i \tag{3.16}$$

Where A corresponds to a vector potential and e to the charge of charge carrier. As we can see that the magnetic field is in Z direction so the electron's motion in the Z direction will remain the same as that of free particle. If we work in Landau gauge A = (-By,0,0) and use conditions [H,p_x]=[H,p_y]=0, then the eigenfunction can be written as:

$$\psi(x, y, z) = exp(ik_z z)exp(ik_x x)\chi(y) \tag{3.17}$$

As a result the energy levels of electrons gets quantised and these quantised energy levels are known as Landau Levels.

$$E_n = \hbar\omega_c(n + \frac{1}{2}) \tag{3.18}$$

where n=0,1,2... and $\omega_c = \frac{eB}{m^*}$. As we can see that the Landau levels are not dependent of (k_x, k_y, k_z) so they are highly degenerate i.e for a single landau level we can have different values of k.

Monolayer

A similar quantisation of energy levels can be seen in the case of graphene. Here the electrons are relativistic and follow the linear dispersion relation. If an external magnetic field is applied perpendicular to the graphene sheet then the Dirac hamiltonian shown in equation 3.13 gets modefied to:

$$H_b = V_F \begin{pmatrix} 0 & -(p_{ox} + ip_{oy}) & 0 & 0 \\ -(p_{ox} - ip_{oy}) & 0 & 0 & \\ 0 & 0 & 0 & (p_{ox} - ip_{oy}) \quad 0 \\ 0 & 0 & (p_{ox} + ip_{oy}) & 0 \end{pmatrix} \tag{3.19}$$

And the corresponding four component wave function:

$$\psi = \begin{pmatrix} \Phi^{K'_A} \\ \Phi^{K'_B} \\ \Phi^{K}_{A} \\ \Phi^{K}_{B} \end{pmatrix} \tag{3.20}$$

As a result the energy level quantisation is given by:

$$E_n = Sgn(n)\sqrt{2e\hbar V_F|n|B} \tag{3.21}$$

where n=. . . -2,-1,0,1,2. . . and V_F = Fermi velocity. The negative values of n corresponds to the valence band and positive to the conduction band. In this case the landau levels are not equidistant with maximum energy gap between zero and first landau level.

Bilayer

For bilayer graphene we use the two-component chiral Hamiltonian h_0 shown in equation 3.15. The information about the magnetic field resides in the operator $p_{oi} = p_i - eA_i$. As we apply a magnetic field perpendicular to the bilayer, we can associate a vector potential A = (0,Bx,0) using landau gauge. This preserves the transnational invariance in the y- direction. As a result the wavefunction takes the form:

$$\phi_l(x,y) = A_l H_l(\frac{x}{\lambda_B} - \frac{p_y\lambda_B}{\hbar})exp[-\frac{1}{2}(\frac{x}{\lambda_B} - \frac{p_y\lambda_B}{\hbar})^2 + i\frac{p_y y}{\hbar}] \tag{3.22}$$

Where $\lambda = \sqrt{\frac{\hbar}{eB}}$ is the magnetic length, H_l are hermite polynomial of order l for integer l lager than 0 and $A_l = \frac{1}{\sqrt{2^l l!\sqrt{\pi}}}$ is a normalisation constant. As a result the energy level quantisation is given by:

$$E_n = Sgn(n)\hbar\omega_c\sqrt{|n|(|n|+1)} \tag{3.23}$$

where ω_c = $\frac{eB}{m^*}$ and n= . . . ,-2,-1,0,1,2. . . .

PMFs as a result of mechanical strain

Experiments have shown that a distortion of the graphene lattice results in massive, nearly uniform Pseudo magnetic fields and Pseudo Landau levels near the Dirac point. [LBM$^+$10]. The linear dispersion relation and triangular symmetry are needed to see such an effect in graphene; otherwise, the synthetic gauge field would not be able to generate a pseudo magnetic field.[Kam20].The quantity A(vector potential corresponding to the pseudo magnetic

field) in the system can vary spatially due to inhomogeneous strain. B = $\boldsymbol{\nabla} \times A$ will produce a pseudo magnetic field, and if A is spatially uniform, curl of A would be zero, resulting in no pseudo magnetic field. [Kam20].

To understand it more vividly, we have to look at the effect of strain on the bond length and the corresponding generation of the strain-induced gauge field.

In the nearest neighbor tight-binding Hamiltonian for graphene

$$\hat{H} = \sum_{<l,m>} \alpha_{lm} C_l^+ C_m \tag{3.24}$$

the carbon-carbon hopping matrix element is α_o= 2.7eV, but as the atoms are displaced relative to each other due to mechanical strain, the bond length changes. As a result, we get a spatially dependent hopping integral.

$$\alpha_{lm} = \alpha(r_l, r_m); r_l = r_l^o + u \tag{3.25}$$

where u is the displacement field.

$$u(x, y) = [u_x(x, y), u_y(x, y), u_z(x, y)] \tag{3.26}$$

The bond length which initially was a_o= 0.142nm changes to d_{lm} = $|r_l - r_m|$ and the corresponding hopping integral α_{lm} is modified to

$$\alpha_{lm} = \alpha_o exp^{-\beta(\frac{d_{lm}}{a_o} - 1)} \tag{3.27}$$

where $\beta = \frac{\partial(log(\alpha))}{\partial(log(a))} \approx 3.87$ at $a = a_o$.

Now by classical continuum mechanics the strain tensor is given by[SA02]:

$$\epsilon_{lm} = \frac{1}{2}(\partial_m u_l + \partial_l u_m + (\partial_l z)(\partial_m z)); l, m = x, y \tag{3.28}$$

As a result, new bond length can also be obtained from the strain tensor:

$$d_{lm} = \frac{1}{a_o}(a_o^2 + \epsilon_{xx} x_l^2{}_m + \epsilon_{xx} y_l^2{}_m + 2\epsilon_{xy} x_{lm}) \tag{3.29}$$

Due to the strain the low energy Dirac Hamiltonian for graphene also gets modified to

$$H(p) = V_F \sigma(p + eA) \tag{3.30}$$

where A can be written as[Mn07]

$$A = \frac{-\hbar\beta}{2ea_o} \begin{pmatrix} \epsilon_{xx} - \epsilon_{yy} \\ -2\epsilon_{xy} \end{pmatrix} \tag{3.31}$$

This strain induced vector potential generates the pseudo magnetic field perpendicular to the graphene sheets.

$$B = \nabla \times A = \partial_x A_y - \partial_y A_x \tag{3.32}$$

The energy level quantization in a series of landau levels as mentioned earlier in the case of graphene is given by:

$$E_n = Sgn(n)\sqrt{2e\hbar V_F |n| B} \tag{3.33}$$

where n=. . . -2,-1,0,1,2. . . and V_F = Fermi velocity.
In the case of bilayer graphene the energy level quantization as mentioned earlier gets modified to:

$$E_n = Sgn(n)\hbar\omega_c\sqrt{|n|(|n|+1)} \tag{3.34}$$

where ω_c = $\frac{eB}{m^*}$ and n= . . . ,-2,-1,0,1,2. . . [**?**]. These landau level quantizations helps us in verifying the experimental data by plotting a graph between E_n vs n(as shown in the next section). Given below are some of the experimental results on strained graphene systems showing generation of pseudo Landau levels as a result of pseudo magnetic field.

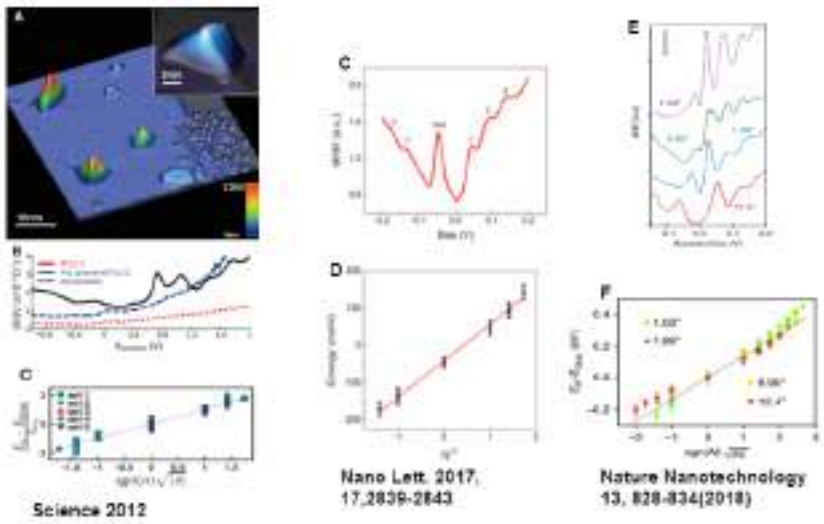

Figure 3.5: Pseudo magnetic field and Landau levels in monolayer graphene under strain.

Similar kind of features are also observed in Bilayer graphene as shown below.

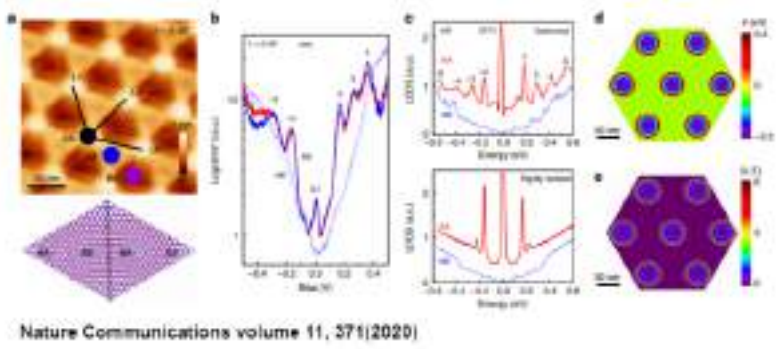

Figure 3.6: Pseudo magnetic field and Landau levels in bilayer graphene

3.3 Sample details and preperation for scanning

This is a new form of multilayer graphene in which each graphene layer is turbostratically decoupled, similar to suspended graphene in nature prepared by Prof.G.U. Kulkarni' Group[MDP$^+$15]. Unlike traditional graphite, where each layer is perfectly AB stacked, in turbostratically single-layer graphene(T-SLG), randomly oriented layers are stacked with undefined order leading to the decoupling of the stacked layers and increased inter-layer distance. Even though the sample is multilayered, the Raman spectra measured on thick flakes show a signature of suspended graphene with a $\frac{I_{2D}}{I_G}$ ratio ranging from 2 to 7·9.

The sample is prepared by spreading naphthalene solution in chloroform on a polycrystalline nickel foil. Joule heating Nickel foil to red hot(800^o) and then cooling it down immediately results in patches of a multilayer of graphene. The inter-layer distance in T-SLG is 3.42 angstroms instead of 3.35 angstroms(results from X-ray diffraction), and the width of the sample is $\sim$ 200nm(300-700 graphene layers).More Details about the sample can be found in Prof. G.U. Kulkarni's paper as Highly Decoupled Graphene Multilayers: Turbostraticity at its Best[MDP$^+$15].

For scanning the sample by STM, it is fixed over a silicon chip with an adhesive(silver-Epoxy). Before putting the sample on scanning, it is first treated by a sample heating facility inside the preparation chamber. We used MATSUSADA PK 20-20 supply at a constant current mode.(current=2A and voltage=1.22volts) for 25-30 minutes. This process is done to remove any impurity on the sample. After cleaning, the sample is transferred to the sample stage for scanning.

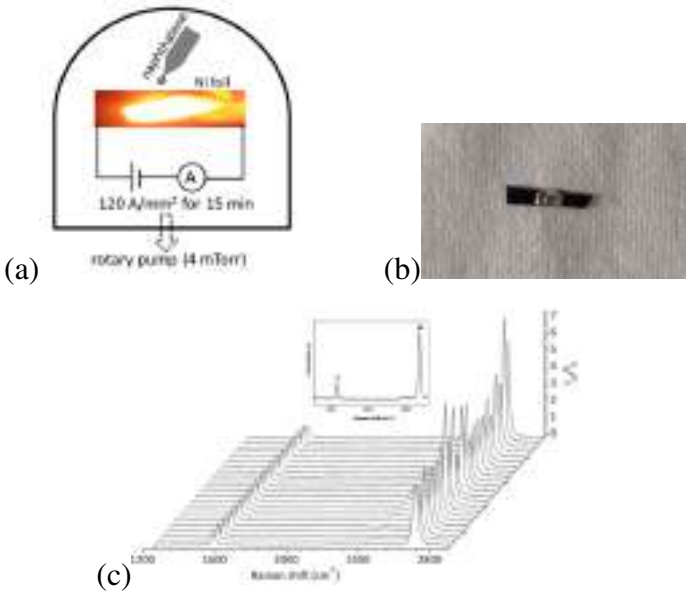

Figure 3.7: (a) Schematic of sample preparation, (b) Sample over a silicon chip, (c) Raman spectra for many samples prepared under identical conditions[MDP+15].Inset shows the Raman spectra of monolayer graphene taken from literature.

3.4 Results from STM

3.4.1 Topographic measurements

Moiré pattern is formed by two overlaying isostructural two-dimensional crystals with slightly different lattice constants or two equivalent crystals deposited on top of each other with a slight misalignment.To get the information about the angles between the layers Moiré patterns are utilized as explained below. A sample of size 0.5cm$\times$0.2cm is cleaned in PC and then it is transferred to the sample stage via EC using a long magnetic manipulator. Figure3.7(a) shows the atomic resolution image of a 10nm$\times$10nm area of the sample. This image was taken at 77Kelvin. The topography shows small hexagonal structure of graphene along with different Moiré patterns(big hexagons of bright spots). To visualize these features more vividly, Fast Fourier Transform(FFT) of the image(figure3.7(b))is performed using Gwyddion software. Masking different regions of FFT image results in a clean image of different features of the sample. Figure3.7(c,d) represents two different types of Moiré pattern having different lattice constants.Two different types of Moiré pattern indicates the contribution from three graphene layers.

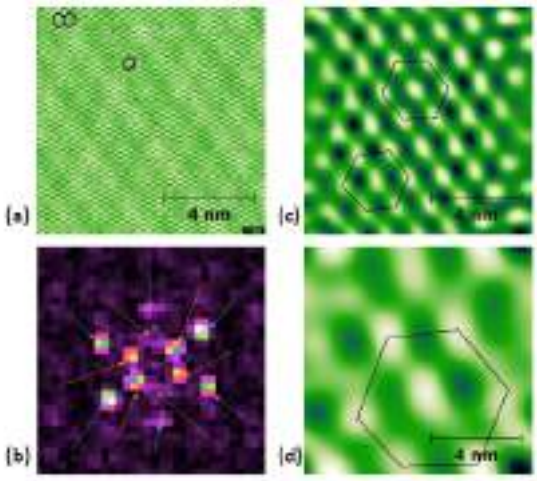

Figure 3.8: **(a) Atomic resolution image at V_B= 350mV and I_{set}= 300pA, (b) Fast Fourier Transform of (a), (c) Real space image corresponding to FFT shown by blue arrows, (d) Real space image corresponding to FFT shown by orange arrows.

These Moiré patterns were further investigated. A python simulation was performed to mimic the mono-layer, bi-layer and tri-layer graphene systems.

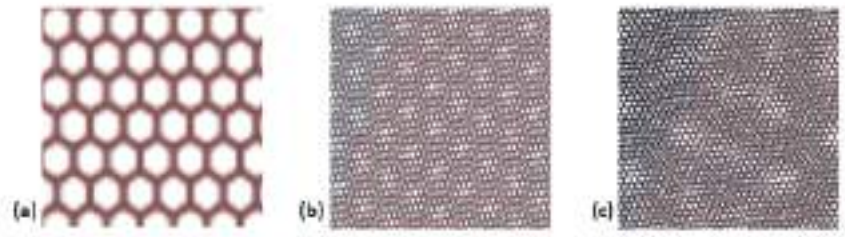

Figure 3.9: (a) Monolayer, (b) Bilayer, (c) Trilayer

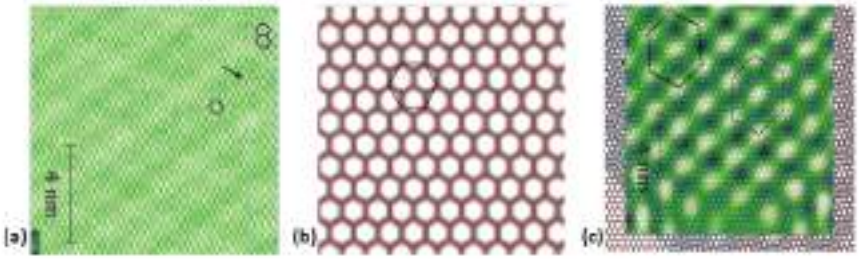

Figure 3.10: **(a) Atomic resolution image with a black hexagon for scaling, (b) Simulate image with a black hexagon for scaling, (c) Superimposed real and simulated image.

The following procedure is followed to find the twist between the layers:

- The real and the simulated images are set at same scale by superimposing the hexagon pointed out by an arrow on left(figure3.9(a)) over the black hexagon on the right in figure3.9(b)

- The scaled real images(FFT filtered) were superimposed over the simulated images of bilayer whose angle of twist were already known.Figure3.9(c) shows the superimposed real and simulated images.

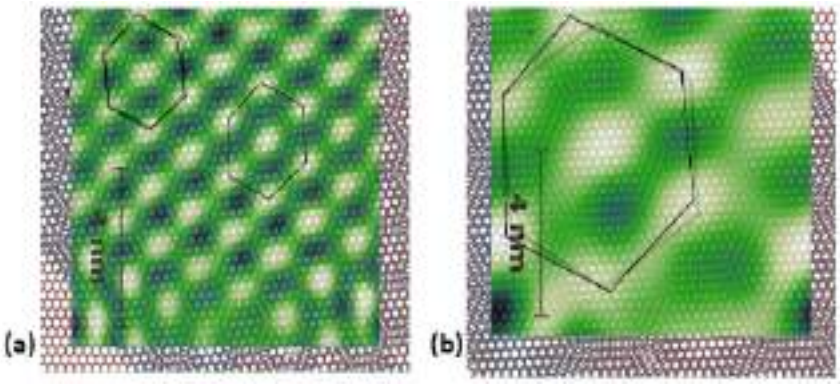

Figure 3.11: (a) The Real and simulated Moiré pattern matches for approximately 11.5^o angle between the two graphene layers, (b) The Real and simulated Moiré pattern match for approximately 4.9^o angle between the two graphene layers.

- By changing the twist between the layers and superimposing it over the real image gives the information about the angle of twist between the sample's graphene layers. It is for the sake of simplicity that only two layers of graphene were involved in the simulation. The results were the same even when three layers of graphene were superimposed.

The twist in the first and second as well as the twist in the second and third layer of graphene was found to be 4.9 and 11.5 degrees respectively.

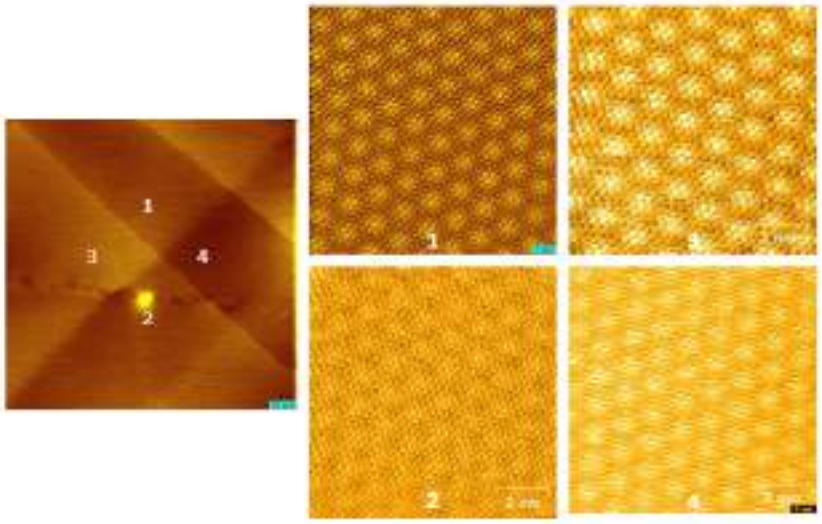

Figure 3.12: †Left most image is of 170nm×170nm area at V_B= 400mV and I_{set}=450pA showing wrinkles and a bright defect. Images 1,2,3 and 4 are of 10nm×10nm V_B= 410mV and I_{set}=450pA area showing Moiré patterns.

Topography of different areas and sizes were taken and investigated as shown in figure3.11. In figure3.11 the left most image was taken for the area of 170nm×170nm. Topography for smaller regions(1,2,3 and 4 figure3.11) was also taken and was found to possess the same angle of twist of 12.2^o. The feature like magic angle was not observed. wrinkles on the sample were clearly seen(image at the center), and spectroscopic analysis was performed on the sample at 77 Kelvin and 300 milliKelvin temperatures.

***Anmol, Ms. Mona and Mr.Soumyadip have 20%,30% and 50% data contribution respectively.*

3.4.2 Spectroscopic measurements

It can be seen in figure 3.11 that wrinkles are present on the sample. To investigate wrinkles more vividly topography and spectroscopy was performed near the wrinkled region at 77 Kelvin temperature. Figure3.12(a) shows the topography of wrinkled area and line spectroscopy was performed at two regions(a) over the wrinkle depicted by red colour(b) over the non wrinkled region depicted by black colour.

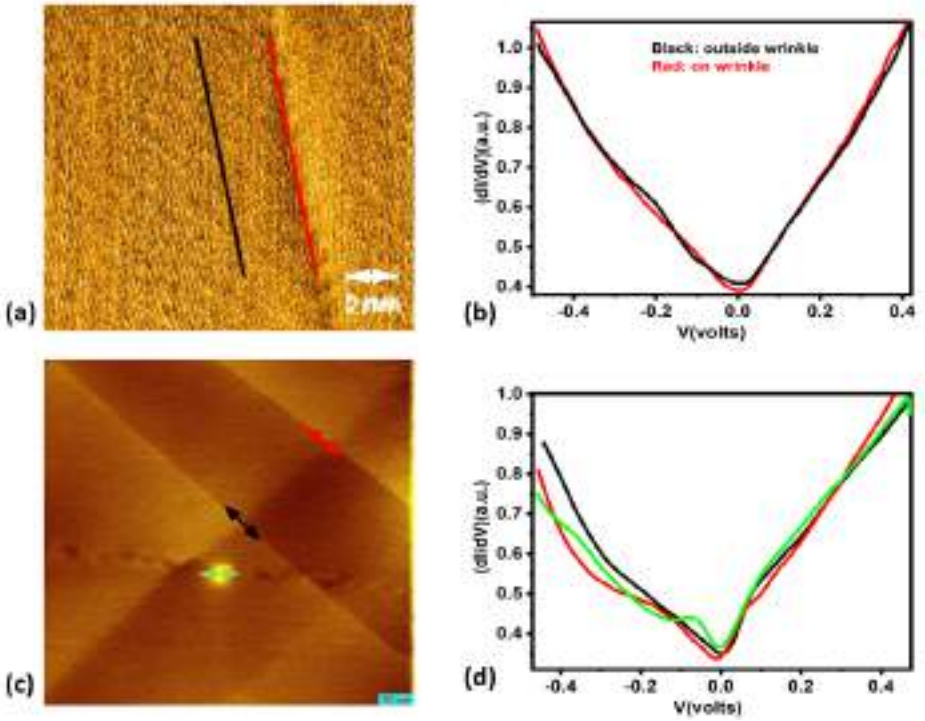

Figure 3.13: †(a) Topography at wrinkled area of $15nm \times 15nm$ at V_B= 350mV and I_{set}=440pA, (b) Line spectroscopy at two different regions, †(c) Topography at wrinkled region of area $170nm \times 170nm$specifying region of line spectroscopy by different colours at V_B= 390mV and I_{set}=450pA, (d) spectroscopy at three different regions indicated by different colours.

It can be seen in figure3.12(b) that the Dirac cone feature is clearly visible in the DOS vs V plot with a zero DOS point corresponding to Dirac point. No difference was observed in the spectroscopy of two different regions.

The region of cross over and defect was analyzed by performing line spectroscopy over the regions at 77Kelvin depicted in figure3.12(c). Spectroscopy at these regions shows

no significant change at 77 Kelvin.(figure3.12(d)) A similar analysis of the sample was performed at 300 milliKelvin temperature. Figure3.13(a) shows the topography over the wrinkle and figure3.13(b) shows the spectroscopy at a point over the wrinkle.

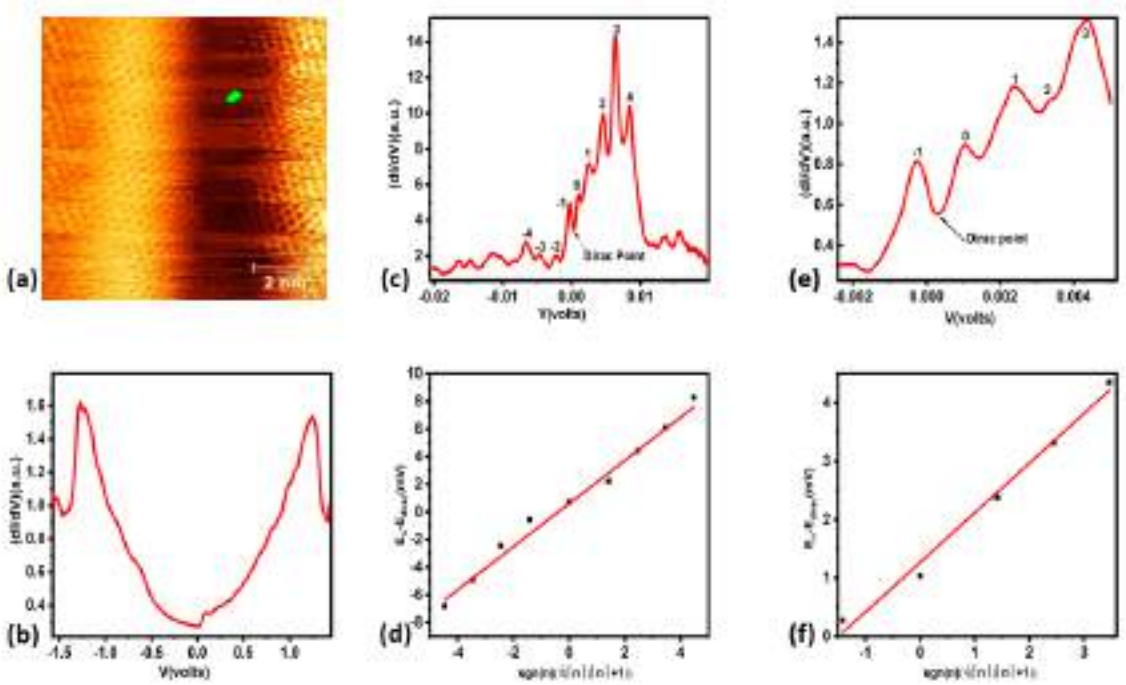

Figure 3.14: †(a)Topography of $10nm \times 10nm$ area at 300mK, (b) spectroscopy at point shown by green mark in (a), *(c)Spectroscopy at lower energy scale showing equally spaced peaks near Dirac point, (d) Plot between $E_n - E_{dirac}$ and $sgn(n)\sqrt{|n|(|n|+1)}$ showing linear variation, *(e)Spectroscopy at lower energy scale showing equally spaced peaks at a region close to wrinkle, (f)Plot between $E_n - E_{dirac}$ and $sgn(n)\sqrt{|n|(|n|+1)}$ showing linear variation

It can be seen that the spectroscopy performed on a wrinkle at 300 millikelvin is different from the data shown at 77Kelvin. To see the features more vividly a spectroscopy at lower energy scale was performed. At this energy scale a series of peaks were observed as shown in figure3.13(c,e). To confirm that these peaks corresponds to the landau level peaks a plot of E_n vs $|n|$ was plotted(as shown in other experiments). It was found that the $E_n - E_{dirac}$ varies linearly with $sgn(n)\sqrt{|n|(|n|+1)}$ as shown in figure3.13(d,f) which is a feature of strain in bilayer graphene(as discussed earlier). In order to estimate the PMF we obtain the slope of the plot $E_n - E_{dirac}$ vs. $sgn(n)\sqrt{|n|(|n|+1)}$ and assume v_F = 1 $\times$ 10^6m/s. Then we put the slope equal to $\hbar\frac{eB}{m*}$(for the use of bilayer). It was found that the field generated

because of this strain is around 3 Tesla. Similarly spectroscopy at a point very close to the wrinkle was performed and similar peaks were observed but less sharp(figure3.13(e)) than the peaks observed at wrinkle. In comparison to the bubble geometry(graphene bubble on Pt(111)), the strain structure realised here allows the strain-induced pseudo magnetic field to be delocalized, allowing it to be detected at distances well beyond the wrinkle. It can be deduced by comparing the two spectroscopic data that figure3.13(e) corresponds to a low strain area and figure3.17(c) corresponds to a high strain area. From the spectroscopic and topographic analysis of the sample it is suspected that the layers are not decoupled near the wrinkles.

† *Anmol and Ms.Deepti have 50-50 data contribution.*

**Anmol and Ms.Deepti have 80% and 20% data contribution respectively.*

3.5 Conclusion

Scanning Tunneling Microscopy was used to perform topography and spectroscopy over turbostratically single layer graphene. Three types of Moiré patterns were found through topography at different regions. Moiré pattern analysis was done, and a twist of 4.9, 11.5 and 12.2 degrees was found in between the layers. The 1.1-degree magic angle was not observed. More topographical analysis needs to be done. Spectroscopy over the wrinkle and near the wrinkle was performed at 77 Kelvin and 300 milliKelvin temperatures. No significant change was observed at the wrinkle and away from the wrinkle at 77 Kelvin.Spectroscopy over the wrinkle at 300 milliKelvin revealed the peaks of Pseudo Landau levels showing consistency with the strain induced pseudo magnetic field. The landau level energy(E_n) was found to vary linearly with $\sqrt{|n|(|n|+1)}$ which signifies that graphene layers are not decoupled at wrinkled regions. The Pseudo magnetic field was found to be delocalized as a result which pseudo landau levels were found even away from the wrinkle .This study offers a quantitative comparison of measured local strain and induced PMF, as well as demonstrating the ability to change the electronic band structure of graphene.. A more detailed analysis of Landau levels can be done in the presence of an external magnetic field, and splitting of landau level peaks can be observed with the increasing magnetic field.

Bibliography

[CNGP+09] A. H. Castro Neto, F. Guinea, N. M. R. Peres, K. S. Novoselov, and A. K. Geim, *The electronic properties of graphene*, Rev. Mod. Phys. **81** (2009), 109–162.

[DAS19] SHEKHAR DAS, *Scanning tunnelling microscopy and transport spectroscopy on candidate topological systems*, Ph.D. thesis, Indian Institute of Science Education and Research, Mohali, 2019.

[Dat20] S. Dattagupta, *Carbon hybridization to tight-binding to dirac solid*, Reson **25** (2020), 249–268.

[Gei07] Novoselov K. Geim, A., *The rise of graphene*, Nature Mater **6** (2007), 183–191.

[Hof03] Jennifer Eve Hoffman, *A search for alternative electronic order in the high temperature superconductor bi2sr2cacu2o8+x by scanning tunneling microscopy*, Ph.D. thesis, University of California, Berkeley, 2003.

[JMD+17] Yuhang Jiang, Jinhai Mao, Junxi Duan, Xinyuan Lai, Kenji Watanabe, Takashi Taniguchi, and Eva Y. Andrei, *Visualizing strain-induced pseudomagnetic fields in graphene through an hbn magnifying glass*, Nano Letters **17** (2017), no. 5, 2839–2843, PMID: 28409936.

[Kam20] Suman Kamboj, *Transport spectroscopy on novel quantum materials*, Ph.D. thesis, Indian Institute of Science Education and Research, Mohali, 2020.

[LBM+10] N. Levy, S. A. Burke, K. L. Meaker, M. Panlasigui, A. Zettl, F. Guinea, A. H. Castro Neto, and M. F. Crommie, *Strain-induced pseudo–magnetic*

fields greater than 300 tesla in graphene nanobubbles, Science **329** (2010), no. 5991, 544–547.

[MDP+15] Umesha Mogera, Radhakrishnan Dhanya, Rajashekhar Pujar, Chandrabhas Narayana, and Giridhar U. Kulkarni, *Highly decoupled graphene multilayers: Turbostraticity at its best*, The Journal of Physical Chemistry Letters **6** (2015), no. 21, 4437–4443, PMID: 26499379.

[MK13] Edward McCann and Mikito Koshino, *The electronic properties of bilayer graphene*, Reports on Progress in Physics **76** (2013), no. 5, 056503.

[Mn07] J. L. Mañes, *Symmetry-based approach to electron-phonon interactions in graphene*, Phys. Rev. B **76** (2007), 045430.

[SA02] Hidekatsu Suzuura and Tsuneya Ando, *Phonons and electron-phonon scattering in carbon nanotubes*, Phys. Rev. B **65** (2002), 235412.